

Temperature-induced optical enhancement near a localization transition

Raul Liquito¹, Miguel Gonçalves², Bruno Amorim¹, Eduardo V. Castro^{1,3}

¹*Centro de Física das Universidades do Minho e do Porto, LaPMET,*

Departamento de Física e Astronomia, Faculdade de Ciências,

Universidade do Porto, Rua do Campo Alegre s/n, 4169-007 Porto, Portugal

²*Princeton Center for Theoretical Science, Princeton University, Princeton NJ 08544, USA and*

³*Beijing Computational Science and Research Center, Beijing 100084, China*

Quasiperiodic systems are an intermediate class of systems between periodic crystals and disordered systems, famously exhibiting metal-insulator transitions (MITs) even in one dimension. While their transport properties have been studied extensively, a systematic analysis of the finite-frequency optical conductivity near the critical point has been lacking. In this work, we carry out a detailed study of the optical conductivity in the paradigmatic Aubry-André model. We find that the zero-temperature low-frequency optical signal is strongly restructured by the quasiperiodic potential, exhibiting an optical gap that closes discontinuously as the system approaches the MIT. Most strikingly, we uncover a mechanism for a strong enhancement of the low-frequency finite temperature optical conductivity at certain resonant frequencies. This enhancement stems from the thermal activation of Pauli-blocked transitions between strongly resonant van Hove singularities. This mechanism provides new insight into finite-frequency transport in quasiperiodic systems and a new pathway for manipulating optical properties near a localization transition. Furthermore, our findings establish the optical response as a powerful, experimentally accessible tool for probing non-trivial quasiperiodicity effects.

I. INTRODUCTION

Quantum systems with quasiperiodic modulations have been a subject of intense study for decades [1, 2]. In disordered systems the absence of translational symmetry leads to the breakdown of Bloch's band theory. In one dimension (1D), any amount of uncorrelated disorder leads to an insulating regime characterized by exponential localization of the eigenfunctions, a phenomena known as Anderson localization [3, 4]. In contrast, translation symmetry breaking in quasiperiodic systems (QPS) can give origin to Bloch-wave-like properties as well as Anderson localization, famously exhibiting metal-insulator transitions (MIT) at a finite potential strength even in one dimension [5]. The exotic properties of these systems, including unique topological features [6–10] and quantum transport properties [11–17] can be experimentally probed in diverse platforms, from optical [18–23] and photonic lattices [8, 24] to moiré materials [25–31].

The Aubry-André model is the paradigmatic example describing a system of non-interacting particles in a 1D lattice subjected to an on-site potential with a quasiperiodic modulation, incommensurate with the underlying lattice. The model hosts a MIT at a critical value of the on-site potential strength. At weak potential strength the system is metallic, with delocalized eigenfunctions and ballistic transport. After the MIT, it enters an insulating/localized regime where the eigenstates become exponentially localized, as in the Anderson model. Exactly at the critical point, the eigenfunctions become multifractal [1, 32, 33] which leads to anomalous transport [34].

Due to the exotic localization and spectral properties of quasiperiodic systems, considerable efforts have been made towards understanding the effects of quasiperiodicity on quantum transport. In Refs. [12, 14] the authors

studied the persistent current by analyzing the system's response under a magnetic flux, showing that throughout the metallic phase the system exhibits a finite persistent current that vanishes in the insulating regime. . Another common approach to transport in quasiperiodic systems is by simulating diffusing wavepackets and extracting the diffusion coefficient for distinct regimes [15, 34, 35] or by performing conductance calculations [36]. In particular, the Aubry-André model exhibits ballistic transport in the extended regime, is insulating in the localized regime and superdiffusive at the critical point. All these methods primarily probe the DC transport properties of the system. Frequency resolved studies of the optical conductivity, on the other hand, have seen little discussion [11, 16, 17, 37]. Significant efforts have been made to adapt Mott's argument to quasiperiodic systems. Mott's original argument for the 1D Anderson model [38] relies on a homogeneous density of states (strong disorder limit) to predict the low-frequency optical conductivity scaling $\sigma(\omega) \propto \omega^2 \ln(\omega/\omega_0)^{d+1}$.

Recent works have successfully modified this approach for specific gapless quasiperiodic system. For instance, in Ref. [11] the authors examine the Maryland model, an exactly solvable system where a nearly diverging quasiperiodic potential induces a smooth, gapless density of states and spectrum-wide Anderson localization. Applying a Mott-like argument yields $\sigma(\omega) \propto e^{-\left(\frac{\omega_0}{\omega}\right)^{1/\sigma}}$. Similarly, in Ref. [17] the author study a modified Aubry-André model with power-law decaying hoppings (exponent $p \geq 2$), finding $\sigma(\omega) \propto \omega^{2-3/p}$.

Extending Mott's argument to standard quasiperiodic systems is fundamentally constrained, since most of these systems, including the Aubry-André model, feature gapped energy spectra that violates the requirement of a homogenous density of states. Thus, a systematic study

of the optical conductivity across the metallic-to-critical regime remains a significant gap in the literature.

In this work we address this gap by demonstrating that the unique spectral properties of the quasiperiodic Aubry-André model give rise to highly tunable and enhanced optical transport features not present in periodic systems. Our primary findings are concisely illustrated in Figs. 1 and 2, where we schematically depict the behavior of the regular part of the absorptive conductivity ($\text{Re}[\sigma_{\text{reg}}(\omega)]$) near the critical point.

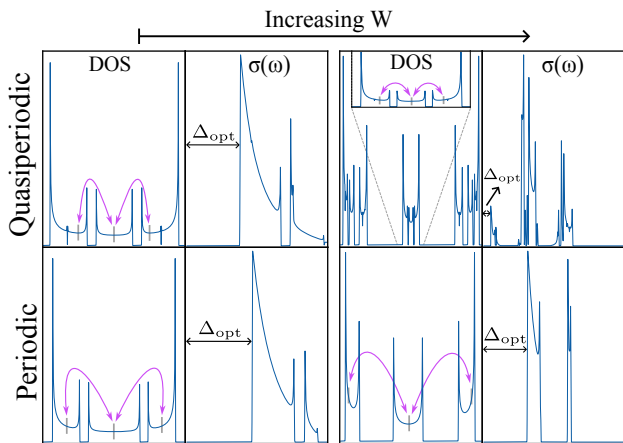


Figure 1. Schematic representation of the regular part of the real optical conductivity as a function of frequency for increasing quasiperiodic potential strength W (left to right). The top row corresponds to the standard Aubry-André model, the bottom row to a purely periodic harmonic modulation with a 55-site unit cell. In the density of states panels (DOS) the purple arrows indicate the transitions associated with the corresponding optical gap Δ_{opt} .

First, we find that the low-frequency behavior of the optical conductivity is strongly modified as we approach the MIT from the extended phase. As schematically illustrated in Fig. 1, this is characterized by strong optical signals at progressively smaller ω , leading to an effectively discontinuous closing of the optical gap Δ_{opt} . This behavior is a consequence of the successive opening of higher order spectral gaps as the critical point is approached, ultimately leading to a fractal spectrum exactly at the critical point. In sharp contrast, a periodic system with approximately the same potential wavelength exhibits a robust and finite optical gap.

Secondly, we uncovered a mechanism for a strong enhancement of the low-frequency optical conductivity upon simply changing the temperature. At zero temperature, transitions between adjacent, gap separated van Hove singularities, are forbidden by Pauli exclusion. However, as depicted in Fig. 2, a finite temperature introduces a thermal occupation imbalance, activating these transitions. This results in the emergence of sharp resonant peaks at finite frequencies (purple and red dots), associated with the energy of the activated van Hove singularities (see the temperature color encoding of Fig. 2).

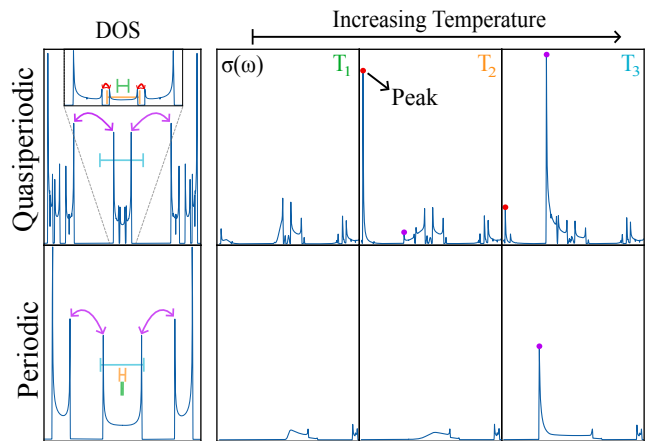


Figure 2. Schematic representation of the regular part of the real optical conductivity as a function of frequency for increasing temperature T (left to right). The top row corresponds to the standard Aubry-André model, the bottom row to a purely periodic harmonic modulation with unit cell enlarged to 55 sites. In the density of states panels (DOS) the purple and red arrows indicate the transitions associated with the corresponding resonance, the spacers show the width of $k_b T$ and are color coded to correspond to their temperatures (top right). The frequency scale is identical across all panels, and the conductivity scale is preserved. Curves correspond to $W = 1.95$ and $T \in \{10^{-4}; 4 \times 10^{-4}; 3.2 \times 10^{-3}\}$.

This effect is strongly enhanced and far more tunable in the quasiperiodic case compared to an periodic approximant system. It is highly sensitive to both temperature and potential strength, which offer two simple knobs to significantly tune the optical response.

The detailed description and in-depth analysis of the mechanism responsible for these observations are provided in the subsequent sections.

This manuscript is organized as follows: in Sec. II we introduce the Aubry-André (AA) model and detail numerical implementations aspects; in Sec. III we provide a concise theoretical introduction to the Kubo-Greenwood formula used for transport calculations; in Sec. IV we present our main findings and provide a detailed analysis of the AA model's optical properties through calculations of DC and AC optical conductivity; in Sec. V we summarize and discuss the main conclusions of this work. We also include an appendix with the following sections: in Appendix. A we derive generic properties of the AA eigenfunctions in the metallic regime using perturbation theory, and obtain the perturbed current matrix elements, establishing a connection with the Drude weight; in Appendix. B we show that at zero temperature the Drude weight is directly determined by the Fermi velocity; in C we calculate the scaling law of the number of states in a van Hove singularity with system size for a generic one-dimensional model (important for understanding the scaling behavior of the optical conductivity in thermal resonances); in Appendix. D we predict the scaling behavior of the optical conductivity in thermal

resonances; in Appendix. E we provide a detailed evolution of the optical conductivity with temperature for two values of potential strength.

II. AUBRY-ANDRÉ MODEL

We consider the Aubry-André (AA) model threaded by a flux θ , which is described the the following Hamiltonian:

$$H = -t \sum_j \left(e^{i\frac{\theta}{L}} c_{j+1}^\dagger c_j + \text{h.c.} \right) + W \sum_j \cos(2\pi\beta j + \phi) c_j^\dagger c_j \quad (1)$$

where L is the number of sites, c_j^\dagger creates an electron at site j , the first term describes hoppings between nearest-neighboring sites, and the second term describes a quasiperiodic potential with strength W and wavenumber $2\pi\beta$. For an irrational β , the single-particle wavefunctions are delocalized for $W < 2t$ and localized for $W > 2t$. The quantum critical point ($W = 2t$) is characterized by a fractal spectrum and multifractal wave functions. The Aubry-André model has a duality between extended and localized phases, by replacing $W \leftrightarrow 2t$, with the critical point $W = 2t$, being self-dual. Through out the manuscript, we will set $\beta = \frac{1+\sqrt{5}}{2}$, the golden mean. .

A. Spectral properties

The Aubry-André model is the paradigmatic example that a fully deterministic potential can also induce a metal-insulator transition. While random disorder tends to wash out spectral features, eventually closing all energy gaps, a quasiperiodic potential instead opens gaps on ever finer energy scales, yielding an increasingly fragmented spectrum that becomes a self-similar Cantor set at the critical point [39].

These complex spectral properties can be understood by considering the potential's effect on the unperturbed Bloch states. In perturbation theory (see Appendix A), the potential couples states with momenta k and $k \pm 2\pi m\beta$.

A simple pedagogical case is the commensurate potential with $\beta = 1/2$, which doubles the unit cell of the system. Here, lowest-order and only coupling ($m = 1$) connects k and $k \pm \pi$, causing band folding at the new Brillouin zone edge ($k = \pm\pi/2$) and opening a gap. Increasing W in this commensurate case renormalizes the energy spectra while keeping the overall periodic structure.

In a truly QPS, all harmonics $m \in \mathbb{Z}$ can in principle contribute. However, the extended/ballistic phase at $W < 2t$ is characterized by a finite correlation length and the support of the eigenfunctions at momenta $k \pm 2\pi m\beta$ decays exponentially with m . Because of this, there is effectively only a finite number of harmonics contributing and therefore a finite number of gaps being opened

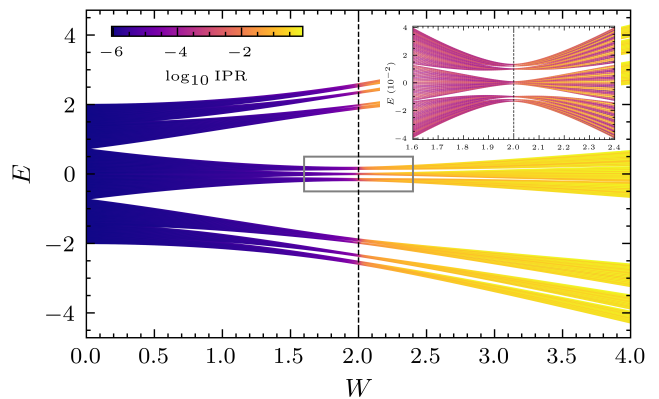


Figure 3. Evolution of AA model energy spectra as a function of quasiperiodic potential strength W for a system size $L = 610$. The inset we plot the same information for a system size $L = 6765$, in the central region highlighted by the grey rectangular box. Notice the different energy (y -axis) scales of the main plot and inset. The color plot encodes the inverse participation ratio (IPR) of each eigenstate. The dashed black vertical line marks the metal-insulator transition of the AA model at $W = 2.0$.

(all higher-order gaps are exponentially suppressed). The resulting energy spectrum in the ballistic regime is therefore a set continuous energy (quasi-Bloch bands), whose dispersion at the band edges remains quadratic, giving rise to the van Hove singularities observed in the density of states (DOS) of the system (Fig. 4). Exactly at the critical point, the correlation length diverges and all harmonics contribute. As a consequence, the eigenfunctions become delocalized in both momentum and real-space.. For $W > 2t$, the eigenstates become exponentially localized in real space (and extended in momentum space) and the correlation length is therefore again finite.

This rich evolution of the energy spectrum with W is shown in Fig. 3. The MIT is evident through the sharp amplitude difference in the inverse participation ratio of the eigenstates, defined for a normalized eigenstate $|\psi_m\rangle = \sum_j \psi_j^m |j\rangle$ as $\text{IPR}_m = \sum_j |\psi_j^m|^4$, where $|j\rangle = c_j^\dagger |0\rangle$. The central focus of this paper is the low-frequency optical response. We will focus at half-filling and on a small energy window around the Fermi level ($E = 0$).

B. Numerical Implementation

We carried out numerical simulations for finite systems with L unit cells. To correctly model the incommensurate limit while using periodic boundary conditions, we use rational approximants. In particular, we set the system size $L = F_n$ (the n -th Fibonacci number) and the potential's inverse wavelength β to be a rational approximant of the golden ratio ($\phi_{GR} = \frac{1+\sqrt{5}}{2}$) given by $\beta_n = F_{n+1}/F_n$. This choice ensures that every finite sys-

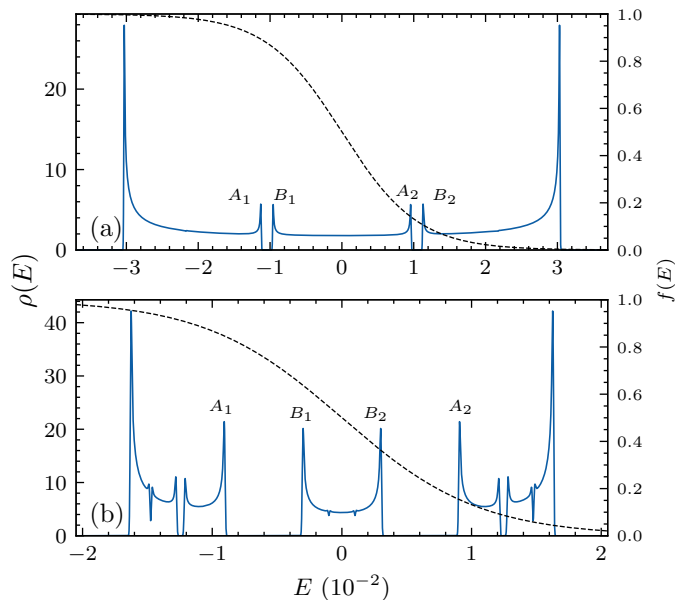


Figure 4. The plots show the DOS of the central bands around $E = 0$. The dotted black curve is the Fermi Dirac function plotted for $T \approx 5 \times 10^{-3}$. Some van Hove singularities are labeled to facilitate the results analysis. The density of states were computed from the exact eigenstates of the AA model for (a) $W = 1.7$ and (b) $W = 1.9$ and for a system size of $L = 28657$.

tem we work with contains exactly a single unit cell.

We also work with a fixed flux $\theta = \pi/2$ and phase shift $\phi = 1/2$ to break time reversal and mirror symmetry lifting all the degeneracies in the spectrum. While such calculations can be averaged over random ensembles of (θ, ϕ) , we find that our main conclusions are robust against changes in phases.

The calculation of the optical response was carried out by evaluating it in terms of eigenstates and eigenenergies of the system. Given that optical conductivity is dominated by eigenenergies close to the Fermi level, only a fraction of the total number of eigenpairs needs to be computed. The eigenpairs close to the Fermi energy ($E = 0$) were obtained using a shift-and-invert spectral transformation alongside a Krylov-Schur subspace method.

III. KUBO-GREENWOOD CONDUCTIVITY

In the non-interacting limit and at low temperatures, where the phonon corrections to the conductivity are negligible, the optical response under an applied electric field can be obtained through the Kubo-Greenwood formula [40, 41]. Written in the eigenbasis of the single-particle equilibrium Hamiltonian, the frequency-dependent optical conductivity $\sigma(\omega)$, which is a scalar for one-dimensional systems, can be written as:

$$\sigma(\omega) = -\frac{i}{L} \sum_{nm} |j_{nm}|^2 \frac{f_n - f_m}{\epsilon_n - \epsilon_m} \frac{1}{\omega + i\eta + \epsilon_n - \epsilon_m}, \quad (2)$$

where we used units with $e = \hbar = a = 1$ where a is the lattice constant, ϵ_n are the energy eigenvalues, $f_n = f(\epsilon_n)$ the corresponding Fermi occupation probabilities, $j_{nm} = \langle \psi_n | \hat{j} | \psi_m \rangle$ the current matrix elements in the eigenbasis representation and η the inverse mean free time / coherence time, accounting for phenomenological dissipation. For computational purposes we choose $\eta \propto L^{-1}$ of the order of the mean level spacing at Fermi level. The conductivity is an intensive property of a material, which can be separated in its regular and singular part. In the limit $\eta \rightarrow 0^+$ it takes the form:

$$\sigma(\omega) = D \left[\pi \delta(\omega) + \frac{i}{\omega} \right] + \sigma_{\text{reg}}(\omega) \quad (3)$$

$$= \sigma_{\text{sing}}(\omega) + \sigma_{\text{reg}}(\omega), \quad (4)$$

where D is the Drude weight (or charge stiffness). Naturally, the Drude weight can be defined through eq. 5 as:

$$D = \lim_{\omega \rightarrow 0} \omega \text{Im} [\sigma(\omega)]. \quad (5)$$

The Drude weight is a key quantity to distinguish between metals, dissipative metals, and insulators [42–46]. In particular, perfect metals have finite Drude weight while insulators have zero Drude peak.

With eq. 2, and by noting that for degenerate states ($\epsilon_n = \epsilon_m$) the term $\frac{f(\epsilon_n) - f(\epsilon_m)}{\epsilon_n - \epsilon_m}$ can be replaced by the derivative $\partial f(\epsilon_n)$, where $\partial f(\epsilon_n) = \left. \frac{\partial f}{\partial \epsilon} \right|_{\epsilon = \epsilon_n}$, we can reach a Fermi level expression for the Drude weight given by

$$D = -\frac{1}{L} \sum_{\substack{nm \\ (\epsilon_n = \epsilon_m)}} |j_{nm}|^2 \partial f(\epsilon_n), \quad (6)$$

where the double sum is restrict to states with the same energy. The singular part of the conductivity $\sigma_{\text{sing}}(\omega)$ is often called an intraband response and it is solely determined by the Drude weight. The real part of the regular conductivity takes the form :

$$\text{Re} [\sigma_{\text{reg}}(\omega)] = -\frac{1}{L} \sum_{\substack{nm \\ (\epsilon_n \neq \epsilon_m)}} |j_{nm}|^2 \frac{f_n - f_m}{\epsilon_n - \epsilon_m} \frac{\eta}{(\omega + \epsilon_n - \epsilon_m)^2 + \eta^2}. \quad (7)$$

and accounts for interband transitions. In the results that follow, we study the transport properties of the Aubry-André model by performing a frequency and temperature resolved study of the Drude weight (D) and real part of the regular conductivity.

IV. RESULTS

We start by establishing the physical energy scales of the model. The Hamiltonian (Eq. 1) is defined by the hopping parameter t , which we set as our unit of energy ($t = 1$). All other quantities, such as temperature T and frequency ω , are therefore expressed in these dimensionless units. To provide a sense of the relevant energy scales, we describe below the temperature and frequency scales associated with typical hopping integrals of $t \approx 1$ eV:

- **Temperature:** A temperature of $T = 1$ corresponds to $k_B T = 1$ eV. This yields $T \approx 11600$ K. The finite temperatures used in our analysis span the range $T \in [10^{-4}, 10^{-3}]$, corresponding to $T \in [1.16, 11.6]$ K.
- **Frequency:** A frequency of $\omega = 1$ corresponds to $\hbar\omega = 1$ eV and therefore to a frequency $\omega \approx 1.52 \times 10^3$ THz. The most relevant spectral features we will study arise for $\omega \in [10^{-3}; 10^{-2}]$, corresponding to $\omega \in [1.52; 15.2]$ THz, placing them in the far-infrared frequency range, and accessible in optical response experimental measurements [47–50].

A. DC conductivity and Drude Weight

We begin by analyzing the DC response, characterized by the Drude weight, D . We recall that in the presence of a scattering time τ , the Drude model conductivity is given by $\sigma(\omega) = D\tau / (1 - i\omega\tau)$, such that the DC conductivity is given by $\sigma_{\text{DC}} = D\tau$. For the metallic phase ($W < 2$), the system is ballistic, and the $T = 0$ Drude weight is directly determined by the Fermi velocity, $D = |v_F|/\pi$ (see Appendix. B for a detailed derivation). Thus, the suppression of the DC conductivity is equivalent to the suppression of the Fermi velocity.

In Fig. 5, we plot the Drude weight D as a function of W , evaluated using three complementary methods that exhibit perfect agreement. The first two methods rely on the zero temperature analytical result $D = |v_F|/\pi$, derived in Appendix. B. In the considered units ($t = \hbar = e = 1$), the Fermi velocity is equivalent to the diagonal current matrix element evaluated at Fermi level $J_{\epsilon_F} = \langle \psi_{\epsilon_F} | \hat{J} | \psi_{\epsilon_F} \rangle$. These two approaches differ exclusively in the numerical procedure employed to determine the Fermi-level eigenstate $|\psi_{\epsilon_F}\rangle$. For the “Real space v_F ” curve, the Hamiltonian matrix is diagonalized in the real space basis, from which the current matrix element is directly computed. Alternatively, the “Perturbation Theory v_F ” method, calculates $|\psi_{\epsilon_F}\rangle$ via a recursive implementation of non-degenerate, time-independent perturbation theory (see Appendix. A 4). For the results presented here, the perturbative expansion is evaluated up to the 100th order. We emphasize that while Kohn’s formula [51] for the Drude weight,

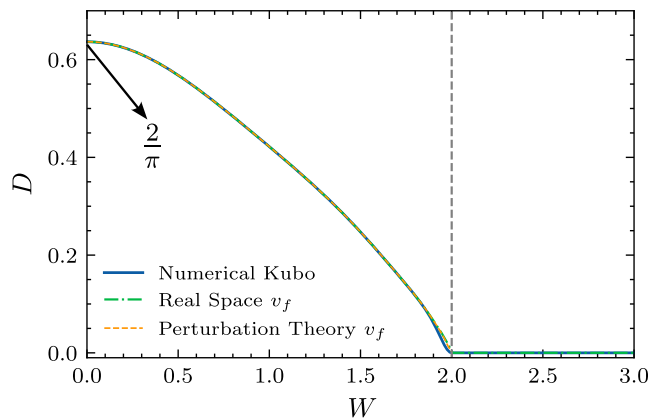


Figure 5. Drude Weight (D) as a function of quasiperiodic potential strength (W) obtained with three different methods. “Numerical Kubo” was obtained for a finite temperature of $T = 5 \times 10^{-4}$, a system size of $L = 10946$ via Krylov-Schur sparse methods. The “Real Space v_F ” was obtained by numerically calculating the eigenstate at Fermi energy ($E = 0$) for a system size $L = 514229$ via via Krylov-Schur sparse methods (see Appendix. B). The “Perturbation Theory v_F ” curve was obtained via perturbation theory for a system size $L = 1597$ truncated to order 100 (see Appendix. A). The dashed grey vertical line marks the metal insulator transition of the AA model at $W = 2$.

$$D \propto \left. \frac{\partial^2 E_0(\theta)}{\partial \theta^2} \right|_{\theta=0} \quad (8)$$

requires the full many-body ground state of the system, our $T = 0$ approach is formally equivalent for systems where the ground state is a Slater determinant. This single-particle formulation offers a significant computational advantage as it strictly requires the eigenstate at the Fermi energy, which can be efficiently obtained utilizing sparse Krylov-Schur eigenvalue solvers.

Lastly, the “Numerical Kubo” method computes the Drude weight utilizing eq. 6. and requires a finite temperature T . Because the energy derivative of the Fermi-Dirac distribution reduces to a Dirac delta function at zero temperature, $\partial f(\epsilon) \rightarrow -\delta(\epsilon - \epsilon_F)$, a direct evaluation of eq. 6 at $T = 0$ is ill-posed. Thus, we evaluate the expression at a small, finite temperature to artificially broaden the delta function. The temperature must be sufficiently large to span several energy levels ($T > S_{\text{ave}}$, where S_{ave} is the mean level spacing around the Fermi level) yet small enough to resolve the relevant energy scales. For the considered system size, we set $T = 5 \times 10^{-4}$, which is approximately S_{ave} . As seen in Fig. 5, this method converges to the direct $T = 0$ calculations.

The monotonic decrease of D in the metallic regime ($W < 2$) is a direct consequence of the effect of the quasiperiodic potential on the band structure. As W increases, the potential induces a hierarchy of gap open-

ings, causing a repulsion between energy bands that in turn lead to the compression of the central band into an ever-narrower energy window. This compression, visible in the spectral evolution in Fig. 3, forces the quasi-Bloch bands to become increasingly flat as $W \rightarrow 2$ and, as a consequence, a smaller v_F and Drude weight.

This behavior is also captured perfectly by perturbation theory. As shown in Appendix. A, the diagonal current matrix elements can be written as Eq. 9:

$$J_k = |c_k|^2 \left(J_k^{(0)} + \sum_{n=1}^{L-1} \sum_{\sigma=\pm 1} \left(\frac{W}{2t} \right)^{2n} |c_{k,\sigma,n}|^2 J_{k+\sigma 2\pi n\beta}^{(0)} \right), \quad (9)$$

where $J_k^{(0)} = 2 \sin(k)$ are the diagonal current matrix elements for the total current in a 1D tight binding chain, $c_{k,\sigma,n}$ are the Bloch amplitudes of the perturbed eigenfunction and c_k the normalization factor (see Appendix. A). These are maximal at $k = \pm\pi/2$, thus near half-filling (where $k_F = \pm\pi/2$). As W increases, weight is transferred from the fundamental harmonic term $J_k^{(0)}$ into its higher-order harmonics $J_{k+\sigma 2\pi n\beta}^{(0)}$ obeying $J_k^{(0)} > J_{k\pm 2\pi n\beta}^{(0)}$, for $k = \pm\pi/2$, leading to a suppression of D with increasing W .

For $W > 2$, the system is in an insulating phase. All eigenstates are exponentially localized, and the Drude weight vanishes ($D = 0$). This is a hallmark of Anderson-type localization [51, 52], as the diagonal current matrix elements for exponentially localized states are suppressed.

These results agree with persistent current calculations in the AA model [12, 14]. In the presence of a magnetic flux θ , the persistent current can be described using a Khon-like formula derived from the Hellman-Feynman theorem Following eq. 8

$$J_\theta = \left\langle \frac{\partial H_\theta}{\partial \theta} \right\rangle = \frac{\partial E_0(\theta)}{\partial \theta} \approx J_0 + D\theta, \quad (10)$$

which follows directly from eq. 8.

B. AC conductivity

In what follows we study the real (absorptive) regular part of conductivity ($\text{Re}[\sigma_{\text{reg}}(\omega)]$) at zero and finite temperature.

1. Zero Temperature ($T = 0$)

In the clean limit ($W = 0$), the real part of $\sigma(\omega)$ exhibits a Drude peak at $\omega \rightarrow 0$ and there are no interband transitions since there is a single energy band. In this limit, we therefore have $\text{Re}[\sigma_{\text{reg}}(\omega)] = 0$. Strictly speaking, the current matrix elements in the eigenbasis are

perfectly diagonal and maximal for states at the Fermi energy. Increasing W within the extended phase leads to the formation of multiple bands of extended states, which we will refer to as quasi-Bloch bands, giving rise to finite interband optical response, as shown in Fig. 6(a).

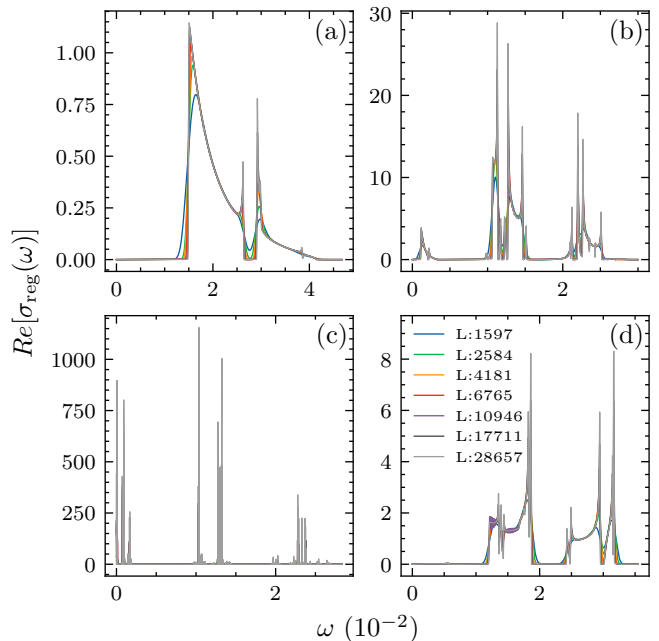


Figure 6. Real part of the regular conductivity ($\text{Re}[\sigma_{\text{reg}}(\omega)]$) as a function of frequency (ω) at zero temperature ($T = 10^{-6}$), for different values of potential strength. Extended phase: (a) $W = 1.8$; (b) $W = 1.95$; Critical point: (c) $W = 2.0$; Localized phase: (d) $W = 2.1$.

Interestingly, the regular part of the conductivity exhibits a clear optical gap ($\Delta_{\text{opt}} = 1.5 \times 10^{-2}$ at $W = 1.8$), which is wider than the central band itself ($\approx 1.2 \times 10^{-2}$ at $W = 1.8$). This gap exists despite a finite DOS at the Fermi energy (see Fig. 4). The existence of a finite optical gap throughout the metallic regime is a clear indication that quasi-Bloch bands behave like conventional Bloch bands, and consequently all intraband finite-frequency transitions below this gap are suppressed.

The evolution of the optical gap as a function of W can be understood through perturbation theory. The quasiperiodic potential causes states to couple and repel, opening energy gaps and producing van Hove singularities like A_1 and B_1 shown in Fig. 4. This intricate structure is governed by two primary properties:

1. **Intraband Decoupling:** states in the same quasi-Bloch band are approximately uncoupled. This is analogous to an effective periodic system with a mini-Brillouin zone (MBZ), where coupled states share the same MBZ crystalline momentum but have different band indexes. Because the current operator is diagonal with respect to the MBZ crystalline momenta, off-diagonal current matrix elements vanish exponentially.

2. Interband Pairwise Resonances: States across a gap (e.g. states near A_1 and B_1) exhibit strong pairwise resonances, leading to off-diagonal matrix elements inversely proportional to their energy separation ($|J_{nm}| \propto (\epsilon_n - \epsilon_m)^{-2}$)[53], see Fig. 7(c).

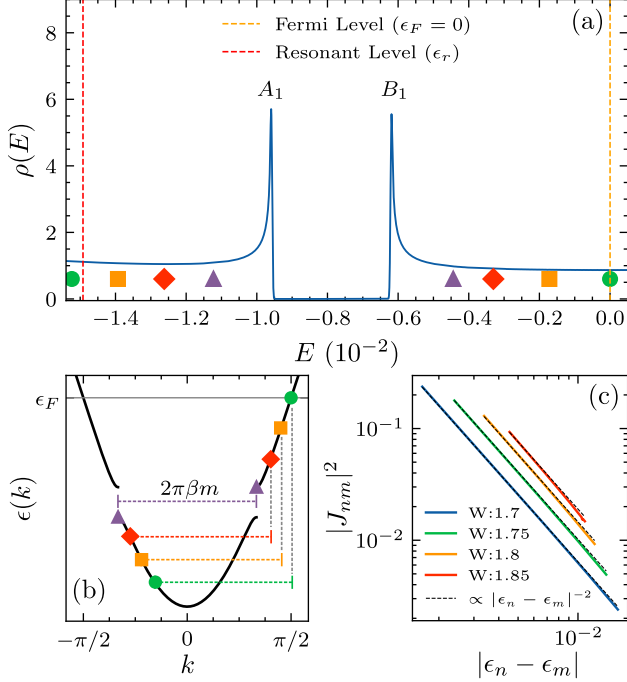


Figure 7. (a) Pairwise resonances around gapped van Hove singularities for $W = 1.8$. The solid blue line represents the DOS, the colored markers correspond to the energy of a few eigenstates around the van Hove singularities. Pairs with the same marker style and color indicate strongly coupled states, i.e., with large $|J_{nm}|$. The dashed vertical lines mark the first resonant states contributing to the zero temperature conductivity. (b) Schematic representation of the quasi-band structure around van Hove singularities and the corresponding pairwise resonances. All the coupled states live in distinct quasi-Bloch bands with a momentum difference of $2\pi\beta m$ for a given $m \in \mathbb{Z}$. (c) Off-diagonal current matrix elements between strongly coupled resonating pairs ($|J_{nm}|^2$) as a function of their energy difference ($|\epsilon_n - \epsilon_m|$) for different values of W . The black dashed lines mark the expected behavior $|J_{nm}|^2 \propto |\epsilon_n - \epsilon_m|^{-2}$.

To better understand the mechanism behind the interband pairwise resonances, consider two quasi-Bloch states with fundamental crystalline momenta k and $k' = k + 2\pi\beta m$ (where $m \in \mathbb{Z}$). In the metallic phase ($W < 2$), higher order harmonics are exponentially suppressed, validating the quasi-Bloch band picture. As the system approaches the critical point, these higher-order harmonics exceed the coupling threshold, causing k and k' to effectively couple. Strong coupling occurs when these pairs are neighbors in k -space ($k' = k \pm \frac{2\pi}{L}$), driving near-divergences in the m -th order perturbation coefficients. This results in level repulsion, gap opening, and the split-

ting of the quasi-band. Furthermore, if k and k' are strongly coupled, the adjacent states $k \pm \frac{2\pi}{L}$ and $k' \mp \frac{2\pi}{L}$ are also strongly coupled, with a perturbation coefficient inversely proportional to the states energy difference.

This intricate pairwise coupling is illustrated in Fig. 7(a-b) and dictates the nature of the optical gap. Because intraband transitions within the central band are suppressed, the first current generating transition must be an interband one. At half-filling, this involves a transition from an occupied neighboring band (e.g. state of energy ϵ_r at A_1 quasi-band) to the Fermi level, leading to an optical gap $\Delta_{\text{opt}} = |\epsilon_r - \epsilon_F|$. Due to the symmetric nature of these resonances, ϵ_r is estimated by matching the number of states between B_1 and the Fermi level with the number of states between A_1 and ϵ_r . This counting scheme provides a formal constraint for ϵ_r :

$$\int_{\epsilon_r}^{\epsilon_{A_1}} \rho(\epsilon) d\epsilon = \int_{\epsilon_{B_1}}^{\epsilon_F} \rho(\epsilon) d\epsilon, \quad (11)$$

where the right-hand side counts the number of states between the Fermi level (ϵ_F) and van Hove singularity B_1 , and the left-hand side counts the number of states between the unknown energy ϵ_r and van Hove singularity A_1 .

As W increases towards the critical point, couplings between k and $k' = k + 2\pi m\beta$, $m \in \mathbb{Z}$ become relevant at progressively higher m , as it is clear from the perturbation theory analysis detailed in Appendix. A. As a consequence, spectral gaps are opened progressively closer to $\omega = 0$ and interband resonances become possible at correspondingly smaller ω , causing an effectively discontinuous decrease in the optical gap Δ_{opt} , as seen in Fig. 6(b). At the critical point (see Fig. 6(c)), the optical gap closes since the spectrum becomes fractal, with gaps opening at all energies. This leads to enhanced conductivity, with resonances proliferating through the whole spectrum.

In the insulating regime (see Fig. 6(d)), the conductivity maintains the overall structure of its dual counterpart, showing a similar gapped structure and optical continuum. Despite the qualitative resemblance, the overall strength of the optical response is smaller due to the localized nature of the eigenfunctions.

In Fig. 8 we plot the optical gap (Δ_{opt}) as a function of W . To compute Δ_{opt} , we consider $\sigma \approx 0$ below a cutoff of $\sigma_\Lambda = 10^{-6} \max[\sigma(\omega)]$. The gap computed in this way evolves through continuous regimes separated by discontinuous jumps that become more frequent as $W \rightarrow 2$, a clear indication of the spectrum fractal nature. As W increases, higher-order terms in the perturbative expansion (see Appendix A) become relevant, effectively opening new gaps within the central band. Each time a new gap opens, the set of allowed transitions changes, causing Δ_{opt} to effectively jump discontinuously. It is however important to clarify what we mean by 'effectively' here. At any finite W , all orders in the perturbative expansion can in principle contribute when the system is quasiperiodic[54]. However, away from the crit-

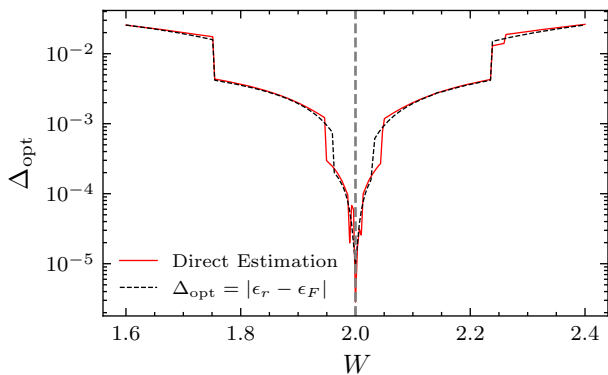


Figure 8. Optical gap (Δ_{opt}) as a function of quasiperiodic potential strength (W) at zero temperature ($T = 10^{-6}$). The red line (“Direct Estimation”) was extracted from the conductivity calculations by imposing a threshold for $\sigma(\omega)$ below which we took as 0. The dotted black line was obtained by calculating ϵ_r following eq. 11.

ical point the correlation length is finite, so gaps generated beyond some order are exponentially suppressed. Consequently, the optical conductivity arising from such higher-order interband processes is nonzero but can be extremely small - below our numerical threshold - thus producing an effective gap.

Finally, Fig. 8 also shows that the behavior of the optical gap is similar around the self-dual point. This follows from the duality of the AA model, which leads to identical gap opening mechanisms in the metallic and insulating phases, with the difference that resonances occur in momentum-space in the former, and in real-space in the latter.

2. Finite Temperature

As discussed previously, states in neighboring gapped van Hove singularities strongly couple in pairs, leading to maximum current matrix elements between states at the edges of each quasi-Bloch band. Despite their strong coupling, these transitions are Pauli blocked at zero temperature and half filling.

The thermal activation of such transitions leads to prominent resonant peaks in conductivity, which diverge in the thermodynamic limit as seen in Fig. 9. This enhancement occurs not only due to the strong current coupling, but also because the states are close in energy and transitions occur between two van Hove singularities, which contribute a large density of states. The strength of the enhancement is controlled by both the temperature and potential strength.

In the insets of Fig. 9 we plot the maximum of the real part of the conductivity as a function of frequency, $\sigma_{\text{peak}} \equiv \max_{\omega} \text{Re}[\sigma_{\text{reg}}(\omega)]$, against the temperature at fixed W . At very low temperature ($T \ll \omega_{\text{peak}}$), the transitions remain effectively Pauli blocked. Increasing

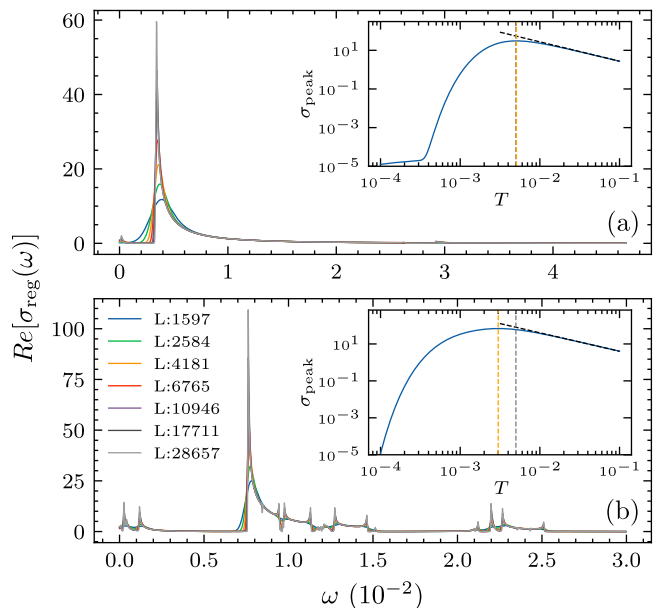


Figure 9. Real part of the regular conductivity ($\text{Re}[\sigma_{\text{reg}}(\omega)]$) as a function of frequency (ω) at zero temperature ($T \approx 5 \times 10^{-3}$), for different values of potential strength. In the insets we plot the value of $\sigma_{\text{peak}} \equiv \max_{\omega} \text{Re}[\sigma_{\text{reg}}(\omega)]$ - the maximum value of the optical conductivity - as a function of temperature (T) for the corresponding potential strength. The orange dashed lines mark the temperature that maximizes σ_{peak} , the gray dashed line marks $T = 5 \times 10^{-3}$, and the black dashed line marks the high temperature T^{-1} behavior. (a) $W = 1.8$; (b) $W = 1.95$.

T increases the optical conductivity until a maximum is reached at $T \approx \omega_{\text{peak}}$, where the thermal energy (T) competes with the transition energy scale. Further increasing T leads to a suppression of the conductivity. This high-temperature algebraic decay ($\sigma_{\text{peak}} \propto T^{-1}$), marked by the dashed black line, can be obtained by expanding the Fermi-Dirac distribution:

$$\frac{f_{A_1} - f_{B_1}}{\epsilon_{A_1} - \epsilon_{B_1}} \approx \left. \frac{\partial f}{\partial \epsilon} \right|_{\epsilon = \epsilon_F} = (4T)^{-1}. \quad (12)$$

The potential strength W also governs the resonance. Increasing W towards the self-dual point allows more terms to contribute to the perturbative expansion thus increasing the current coupling between the pairs, and leading to an increased optical response. Concurrently, the energy spectra is compressed into narrower energy windows, lowering the optimal resonance temperature: at $W = 1.8$, the maximum resonance occurs at $T \approx 5 \times 10^{-3}$ as shown in Fig. 9(a), but at $W = 1.95$ it occurs at $T \approx 2 \times 10^{-3}$, as shown in Fig. 9(b).

Despite the narrowing of the quasi-Bloch bands, the resonant frequency increases monotonically as W approaches the critical point, as seen in Fig. 10(b). This appears to contradict the compression mechanism, however, as the energy spectra is compressed, the increasing resonance

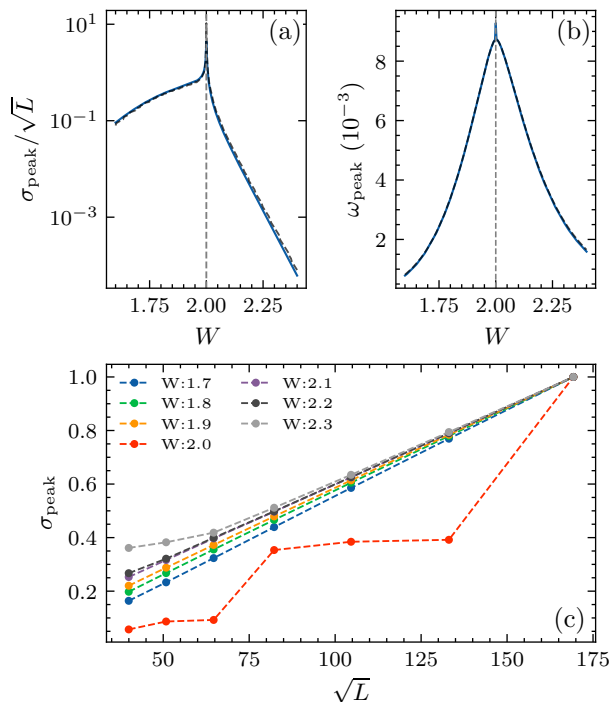


Figure 10. **(a)** Height of the conductivity peak ($\sigma_{\text{peak}} \equiv \max_{\omega} \text{Re}[\sigma_{\text{reg}}(\omega)]$) as a function of potential strength (W) for a system with $L = 28657$. The solid line was extracted from the conductivity data, the dashed line is a naive estimation done by explicitly summing the Kubo-Greenwood expression for the conductivity (see Appendix. D). **(b)** Frequency of conductivity peak (ω_{peak}) as a function of potential strength (W) for a system with $L = 28657$. The solid line was extracted from the conductivity data and was obtained by mapping the position of the resonant van Hove singularity and computing their energy difference. **(c)** Height of the conductivity peak (σ_{peak}) as a function of \sqrt{L} for different potential strengths (W). The data points correspond to $L \in \{1597, 2584, 4181, 6765, 10946, 17711, 28657\}$.

between van Hove singularity pairs is accompanied by an increasing repulsion, thus increasing the energy distance between the van Hove singularities. This can be promptly observed in the DOS in Fig. 4.

Into the localized regime, the resonance is suppressed with increasing W , as seen in Fig. 10(a). This is a clear signature of the exponentially localized eigenfunctions. In the strong potential limit, the localization length ξ is of the order of the lattice spacing a and the current matrix elements are suppressed with increasing potential strength.

In Fig. 10(c), we plot the height of the peak σ_{peak} as a function of \sqrt{L} where L is the tight-binding chain size. With the exception of $W = 2.0$ (self-dual point), the \sqrt{L} scaling is evident indicating an intricate connection with the number of states in each van Hove singularity, proportional to \sqrt{L} (see appendix C). This stems from the pairwise resonance structure around gapped van Hove singularities. Each state resonates uniquely with its pair,

leading to a total of number of current generating transitions equal to the number of states in a van Hove singularity, which is proportional to \sqrt{L} . It is important to note that throughout this work we chose $\eta \propto L^{-1}$, proportional to the mean level spacing at Fermi level, thus inducing the \sqrt{L} divergence. In fact, the resonance peaks scale as $\sigma_{\text{peak}} \propto \eta^{-1/2}$, as shown in Appendix. D, where is set η is set physically by a finite coherence time of the sample. Because of this, no true divergences are expected in experiment.

V. CONCLUSION

In this work, we performed a systematic study of the optical conductivity near the metal-insulator transition of the one-dimensional Aubry-André (AA) model.

Our analysis of the DC response demonstrated an efficient zero temperature method to compute the Drude weight (D) from a single eigenstate at the Fermi energy, enabling simulations of large-scale systems (up to millions of

sites). This real-space approach, shown to be equivalent to perturbative calculations of the Fermi velocity, confirms that D is suppressed as $W \rightarrow 2$ due to the progressive flattening of the quasi-Bloch bands. Our findings are in excellent agreement with previous persistent current calculations [12, 14].

At finite frequencies, the $T = 0$ optical response serves as a powerful probe of the model's unique spectral properties. In sharp contrast to comparable periodic systems, we found that the optical gap Δ_{opt} is not robust under increasing potential strength. Instead, it closes effectively discontinuously as the system approaches the critical point, a direct consequence of the emerging fractal, Cantor-set-like energy spectrum.

Strikingly, we observed a mechanism for strong optical enhancement driven by finite temperature. As T increases, the thermal occupation imbalance activates previously Pauli-blocked transitions between strongly coupled, gap-separated van Hove singularities. This results in sharp, prominent resonant peaks in the far-infrared conductivity. This effect is substantially more pronounced and tunable in the quasiperiodic limit than in the periodic counterpart, providing a platform where the resonance frequency can be precisely controlled by both potential strength W and temperature T .

This mechanism provides new insight into the impact of quasiperiodicity on finite-frequency transport and offers a new pathway for manipulating optical properties near a localization transition. While demonstrated for the AA model, we expect this phenomenon to be a general feature of more generic 1D quasiperiodic systems. Finally, our results identify the optical response as a powerful experimental tool for probing quasiperiodicity, with predictions directly testable in platforms such as ultracold atoms in optical lattices [19, 22].

ACKNOWLEDGMENTS

R.L. acknowledges funding from Fundação para a Ciência e Tecnologia (FCT-Portugal) through Grant No. 2024.01276.BD. MG is supported by a postdoctoral research fellowship at the Princeton Center for Theoretical Science. We also acknowledge the Tianhe-2JK cluster at the Beijing Computational Science Research Center (CSRC), the OBLIVION and VISION super-

computer, Navigator cluster and the Deucalion cluster through Projects No. 2022.15834.CPCA.A1 and No. 2022.15910.CPCA.A1 (based at the High Performance Computing Center—University of Évora) funded by the ENGAGE SKA Research Infrastructure (Reference No. POCI-01-0145-FEDER-022217—COMPETE 2020 and the Foundation for Science and Technology, Portugal) and by the BigData@UE project (Reference No. ALT20-03-0246-FEDER-000033—FEDER) and the Alentejo 2020 Regional Operational Program.

-
- [1] M. Kohmoto, B. Sutherland, and C. Tang, Critical wave functions and a Cantor-set spectrum of a one-dimensional quasicrystal model, *Phys. Rev. B* **35**, 1020 (1987).
- [2] A. I. Goldman and R. F. Kelton, Quasicrystals and crystalline approximants, *Rev. Mod. Phys.* **65**, 213 (1993).
- [3] P. W. Anderson, Absence of Diffusion in Certain Random Lattices, *Phys. Rev.* **109**, 1492 (1958).
- [4] A. MacKinnon and B. Kramer, One-Parameter Scaling of Localization Length and Conductance in Disordered Systems, *Phys. Rev. Lett.* **47**, 1546 (1981).
- [5] S. Aubry and G. André, Analyticity breaking and Anderson localization in incommensurate lattices, *Ann. Israel Phys. Soc* **3**, 18 (1980).
- [6] Y. E. Kraus, Y. Lahini, Z. Ringel, M. Verbin, and O. Zeitler, Topological States and Adiabatic Pumping in Quasicrystals, *Phys. Rev. Lett.* **109**, 106402 (2012).
- [7] Y. E. Kraus and O. Zeitler, Topological Equivalence between the Fibonacci Quasicrystal and the Harper Model, *Phys. Rev. Lett.* **109**, 116404 (2012).
- [8] M. Verbin, O. Zeitler, Y. E. Kraus, Y. Lahini, and Y. Silberberg, Observation of Topological Phase Transitions in Photonic Quasicrystals, *Phys. Rev. Lett.* **110**, 076403 (2013).
- [9] R. Liquito, M. Gonçalves, and E. V. Castro, Fate of quadratic band crossing under quasiperiodic modulation, *Phys. Rev. B* **109**, 174202 (2024).
- [10] R. Liquito, M. Gonçalves, and E. Castro, Quasiperiodic quadrupole insulators, *SciPost Physics* **18**, 208 (2025).
- [11] R. E. Prange, D. R. Grempel, and S. Fishman, Long-Range Resonance in Anderson Insulators: Finite-Frequency Conductivity of Random and Incommensurate Systems, *Phys. Rev. Lett.* **53**, 1582 (1984).
- [12] N. Roy and S. Sinha, A finite temperature study of ideal quantum gases in the presence of one dimensional quasiperiodic potential, *J. Stat. Mech.* **2018**, 053106 (2018).
- [13] G. Roósz, U. Divakaran, H. Rieger, and F. Iglói, Nonequilibrium quantum relaxation across a localization-delocalization transition, *Phys. Rev. B* **90**, 184202 (2014).
- [14] N. Roy and A. Sharma, Study of counterintuitive transport properties in the Aubry-André-Harper model via entanglement entropy and persistent current, *Phys. Rev. B* **100**, 195143 (2019), [arXiv:1905.13255 \[cond-mat\]](https://arxiv.org/abs/1905.13255).
- [15] D. S. Bhakuni, T. L. M. Lezama, and Y. Bar Lev, Noise-induced transport in the Aubry-André-Harper model, *SciPost Phys. Core* **7**, 023 (2024).
- [16] A. Lahiri, Ac conductivity of incommensurate lattices: Anatomy of wave functions, *Phys. Rev. B* **53**, 3702 (1996).
- [17] S. Gopalakrishnan, Self-dual quasiperiodic systems with power-law hopping, *Phys. Rev. B* **96**, 054202 (2017), [arXiv:1706.05382 \[cond-mat\]](https://arxiv.org/abs/1706.05382).
- [18] G. Roati, C. D’Errico, L. Fallani, M. Fattori, C. Fort, M. Zaccanti, G. Modugno, M. Modugno, and M. Inguscio, Anderson localization of a non-interacting Bose-Einstein condensate, *Nature* **453**, 895 (2008).
- [19] M. Modugno, Exponential localization in one-dimensional quasi-periodic optical lattices, *New J. Phys.* **11**, 033023 (2009).
- [20] M. Schreiber, S. S. Hodgman, P. Bordia, H. P. Lüschen, M. H. Fischer, R. Vosk, E. Altman, U. Schneider, and I. Bloch, Observation of many-body localization of interacting fermions in a quasirandom optical lattice, *Science* **349**, 842 (2015).
- [21] H. P. Lüschen, P. Bordia, S. Scherg, F. Alet, E. Altman, U. Schneider, and I. Bloch, Observation of Slow Dynamics near the Many-Body Localization Transition in One-Dimensional Quasiperiodic Systems, *Phys. Rev. Lett.* **119**, 260401 (2017).
- [22] R. Anderson, F. Wang, P. Xu, V. Venu, S. Trotzky, F. Chevy, and J. H. Thywissen, Conductivity Spectrum of Ultracold Atoms in an Optical Lattice, *Phys. Rev. Lett.* **122**, 153602 (2019).
- [23] W. G. T. Kamkou, N. Tchepemen, and J. P. Nguenang, Spectral and dynamical characters of 1D incommensurate optical lattices with PT-symmetry, *Physica B: Condensed Matter* **667**, 415130 (2023).
- [24] Y. Lahini, R. Pugatch, F. Pozzi, M. Sorel, R. Morandotti, N. Davidson, and Y. Silberberg, Observation of a Localization Transition in Quasiperiodic Photonic Lattices, *Phys. Rev. Lett.* **103**, 013901 (2009).
- [25] Moiré magic three years on, *Nat Rev Mater* **6**, 191 (2021).
- [26] P. Moon, M. Koshino, and Y.-W. Son, Quasicrystalline electronic states in $\{30\}^{\circ}$ rotated twisted bilayer graphene, *Phys. Rev. B* **99**, 165430 (2019).
- [27] G. Yu, Z. Wu, Z. Zhan, M. I. Katsnelson, and S. Yuan, Dodecagonal bilayer graphene quasicrystal and its approximants, *npj Comput Mater* **5**, 1 (2019).
- [28] S. Pezzini, V. Mišeiškis, G. Piccinini, S. Forti, S. Pace, R. Engelke, F. Rossella, K. Watanabe, T. Taniguchi, P. Kim, and C. Coletti, 30° -Twisted Bilayer Graphene Quasicrystals from Chemical Vapor Deposition, *Nano Lett* **20**, 3313 (2020).
- [29] M. Gonçalves, H. Z. Olyaei, B. Amorim, R. Mondaini, P. Ribeiro, and E. V. Castro, Incommensurability-induced sub-ballistic narrow-band-states in twisted bilayer graphene, *2D Mater.* **9**, 011001 (2021).

- [30] A. Uri, S. C. de la Barrera, M. T. Randeria, D. Rodan-Legrain, T. Devakul, P. J. D. Crowley, N. Paul, K. Watanabe, T. Taniguchi, R. Lifshitz, L. Fu, R. C. Ashoori, and P. Jarillo-Herrero, Superconductivity and strong interactions in a tunable moiré quasicrystal, *Nature* **620**, 762 (2023).
- [31] X. Lai, D. Guerci, G. Li, K. Watanabe, T. Taniguchi, J. Wilson, J. H. Pixley, and E. Y. Andrei, *Imaging Self-aligned Moiré Crystals and Quasicrystals in Magic-angle Bilayer Graphene on hBN Heterostructures* (2023), [arXiv:2311.07819 \[cond-mat\]](https://arxiv.org/abs/2311.07819).
- [32] M. Gonçalves, B. Amorim, E. V. Castro, and P. Ribeiro, Critical Phase Dualities in 1D Exactly Solvable Quasiperiodic Models, *Phys. Rev. Lett.* **131**, 186303 (2023).
- [33] R. Oliveira, N. Sobrosa, P. Ribeiro, B. Amorim, and E. V. Castro, *Local Density of States as a Probe of Multifractality in Quasiperiodic Moiré Materials* (2025), [arXiv:2510.20575 \[cond-mat\]](https://arxiv.org/abs/2510.20575).
- [34] A. Purkayastha, S. Sanyal, A. Dhar, and M. Kulkarni, Anomalous transport in the Aubry-André-Harper model in isolated and open systems, *Phys. Rev. B* **97**, 174206 (2018).
- [35] Y. Bar Lev, D. M. Kennes, C. Klöckner, D. R. Reichman, and C. Karrasch, Transport in quasiperiodic interacting systems: From superdiffusion to subdiffusion, *EPL* **119**, 37003 (2017).
- [36] J. Sutradhar, S. Mukerjee, R. Pandit, and S. Banerjee, Transport, multifractality, and the breakdown of single-parameter scaling at the localization transition in quasiperiodic systems, *Phys. Rev. B* **99**, 224204 (2019), [arXiv:1810.12931 \[cond-mat\]](https://arxiv.org/abs/1810.12931).
- [37] H. Iijima, Y. Murakami, and A. Koga, Optical Response of the Tightbinding Model on the Fibonacci Chain, *J. Phys. Soc. Jpn.* **91**, 124702 (2022).
- [38] N. F. Mott, Conduction in non-crystalline materials: III. Localized states in a pseudogap and near extremities of conduction and valence bands, *The Philosophical Magazine: A Journal of Theoretical Experimental and Applied Physics* **19**, 835 (1969).
- [39] A. Avila and S. Jitomirskaya, The Ten Martini Problem, *Ann. Math.* **170**, 303 (2009).
- [40] R. Kubo, Statistical-Mechanical Theory of Irreversible Processes. I. General Theory and Simple Applications to Magnetic and Conduction Problems, *J. Phys. Soc. Jpn.* **12**, 570 (1957).
- [41] D. A. Greenwood, The Boltzmann Equation in the Theory of Electrical Conduction in Metals, *Proc. Phys. Soc.* **71**, 585 (1958).
- [42] I. Souza, T. Wilkens, and R. M. Martin, Polarization and localization in insulators: Generating function approach, *Phys. Rev. B* **62**, 1666 (2000).
- [43] R. Resta, Why are insulators insulating and metals conducting?, *J. Phys.: Condens. Matter* **14**, R625 (2002).
- [44] R. Resta, Drude weight and superconducting weight, *J. Phys.: Condens. Matter* **30**, 414001 (2018).
- [45] P. Drude, Zur Elektronentheorie der Metalle, *Annalen der Physik* **306**, 566 (1900).
- [46] D. J. Scalapino, S. R. White, and S. Zhang, Insulator, metal, or superconductor: The criteria, *Phys. Rev. B* **47**, 7995 (1993).
- [47] J. Zhang, X. Chen, S. Mills, T. Ciavatti, Z. Yao, R. Mescall, H. Hu, V. Semenenko, Z. Fei, H. Li, V. Perebeinos, H. Tao, Q. Dai, X. Du, and M. Liu, Terahertz Nanoimaging of Graphene, *ACS Photonics* **5**, 2645 (2018).
- [48] R. Jing, Y. Shao, Z. Fei, C. F. B. Lo, R. A. Vitalone, F. L. Ruta, J. Staunton, W. J.-C. Zheng, A. S. Mcleod, Z. Sun, B.-y. Jiang, X. Chen, M. M. Fogler, A. J. Millis, M. Liu, D. H. Cobden, X. Xu, and D. N. Basov, Terahertz response of monolayer and few-layer WTe₂ at the nanoscale, *Nat Commun* **12**, 5594 (2021).
- [49] X. Guo, K. Bertling, B. C. Donose, M. Brünig, A. Cernescu, A. A. Govyadinov, and A. D. Rakić, Terahertz nanoscopy: Advances, challenges, and the road ahead, *Applied Physics Reviews* **11**, 021306 (2024).
- [50] S.-D. Chen, Q. Feng, W. Zhao, R. Qi, Z. Zhang, D. Abeysinghe, C. Uzundal, J. Xie, T. Taniguchi, K. Watanabe, and F. Wang, Direct measurement of terahertz conductivity in a gated monolayer semiconductor, <https://arxiv.org/abs/2409.17633v1> (2024).
- [51] W. Kohn, Theory of the Insulating State, *Phys. Rev.* **133**, A171 (1964).
- [52] D. Thouless, Electrons in disordered systems and the theory of localization, *Physics Reports* **13**, 93 (1974).
- [53] This holds for resonating pairs around gapped van Hove singularities.
- [54] Note that within the localized phase ($W > 2$), a large W perturbative expansion can also be carried out, treating the hopping as a perturbation. In this case, gap openings are induced by real-space resonances (and not momentum-space resonances like in the extended phase).
- [55] J. J. Sakurai and J. Napolitano, *Modern Quantum Mechanics*, 3rd ed. (Cambridge University Press, Cambridge, 2021).

Appendix A: Perturbation Theory in the AA model

We treat the AA model (eq. 1) using standard non-degenerate perturbation theory for $W < 2t$. The unperturbed Hamiltonian H_0 is the 1D tight-binding model, and the perturbation is the quasiperiodic potential, $\hat{V} = W \sum_x \cos(2\pi\beta x + \phi) |x\rangle \langle x|$.

1. Perturbed Eigenstates and Energies

In the unperturbed Bloch basis $|\psi_k^{(0)}\rangle$, the perturbation matrix elements are:

$$\langle \psi_{k'}^{(0)} | \hat{V} | \psi_k^{(0)} \rangle = \frac{W}{2} (\delta_{k+2\pi\beta, k'} + \delta_{k-2\pi\beta, k'}). \quad (\text{A1})$$

This shows that the perturbation only couples states with momenta k and $k \pm 2\pi\beta$.

The first-order energy correction is zero: $\Delta_k^{(1)} = V_{kk} = 0$. The second-order correction is

$$\Delta_k^{(2)} = \sum_{k' \neq k} \frac{|V_{kk'}|^2}{\epsilon_k^{(0)} - \epsilon_{k'}^{(0)}} = \left(\frac{W}{2}\right)^2 \sum_{\sigma=\pm 1} \frac{1}{\epsilon_k^{(0)} - \epsilon_{k+\sigma 2\pi\beta}^{(0)}} \quad (\text{A2})$$

The first-order correction to the wavefunction is:

$$|\psi_k^{(1)}\rangle = \sum_{k' \neq k} \frac{V_{k'k}}{\epsilon_k^{(0)} - \epsilon_{k'}^{(0)}} |\psi_{k'}^{(0)}\rangle = \frac{W}{2} \sum_{\sigma=\pm 1} \frac{1}{\epsilon_k^{(0)} - \epsilon_{k+\sigma 2\pi\beta}^{(0)}} |\psi_{k+\sigma 2\pi\beta}^{(0)}\rangle. \quad (\text{A3})$$

The second-order correction to the wavefunction, $|\psi_k^{(2)}\rangle$, couples to states $|\psi_{k\pm 4\pi\beta}^{(0)}\rangle$. All odd-order energy corrections are zero, as they require returning to the original k -state, which involves an even number of potential couplings.

This process generates a perturbative expansion where the n -th order wavefunction correction, $|\psi_k^{(n)}\rangle$, couples the unperturbed state $|\psi_k^{(0)}\rangle$ to its n -th order harmonics, $|\psi_{k\pm 2\pi n\beta}^{(0)}\rangle$, as well as lower-order harmonics via more complex k -paths.

The full (unnormalized) quasi-Bloch state can be written structurally as:

$$|\psi_k\rangle \propto |\psi_k^{(0)}\rangle + \sum_{n=1}^{+\infty} \left(\frac{W}{2}\right)^n \sum_{\sigma=\pm 1} \left(c_{k,\sigma,n}^{(n)} |\psi_{k+\sigma 2\pi n\beta}^{(0)}\rangle + \sum_{m < n} c_{k,\sigma,m}^{(n)} |\psi_{k+\sigma 2\pi m\beta}^{(0)}\rangle \right), \quad (\text{A4})$$

where the coefficients $c_{k,\sigma,n}^{(n)} = \prod_{m=1}^n \frac{1}{\epsilon_k^{(0)} - \epsilon_{k+\sigma 2\pi m\beta}^{(0)}}$ come from trivial k -space paths, and $c_{k,\sigma,m}^{(n)}$ measure the coupling to lower-order harmonics. Thus the coefficients $c_{k,\sigma,m}^{(n)}$ represent the n -th correction to the m -th order harmonic. From $\Delta_k^{(n)} = \langle \psi_k^{(0)} | \hat{V} | \psi_k^{(n-1)} \rangle$, the full energy correction is:

$$\epsilon_k \approx \epsilon_k^{(0)} + \sum_n \sum_{\sigma=\pm 1} \left(\frac{W}{2}\right)^{2n} c_{k,\sigma,1}^{(2n-1)}. \quad (\text{A5})$$

The full unnormalized quasi-Bloch state can be rewritten as a plane wave expansion by grouping all m -th order corrections into a single coefficient:

$$|\psi_k\rangle \propto |\psi_k^{(0)}\rangle + \sum_n \sum_{\sigma=\pm 1} \left(\frac{W}{2}\right)^n c_{k,\sigma,n} |\psi_{k+\sigma 2\pi n\beta}^{(0)}\rangle \quad (\text{A6})$$

$$c_{k,\sigma,n} = c_{k,\sigma,n}^{(n)} + \sum_{m>n} \left(\frac{W}{2}\right)^{m-n} c_{k,\sigma,n}^{(m)} \quad (\text{A7})$$

The normalized quasi-Bloch state is then:

$$|\psi_k\rangle = c_k |\psi_k^{(0)}\rangle + \sum_n \sum_{\sigma=\pm 1} \left(\frac{W}{2}\right)^n \tilde{c}_{k,\sigma,n} |\psi_{k+\sigma 2\pi n\beta}^{(0)}\rangle \quad (\text{A8})$$

where $c_k = \left(1 + \sum_n \left(\frac{W}{2}\right)^{2n} |c_{k,\sigma,n}|^2\right)^{-1/2}$ is the normalization factor (the weight of the original Bloch state) and $\tilde{c}_{k,\sigma,n} = c_k c_{k,\sigma,n}$ are the normalized coefficients for the harmonics.

2. Current Matrix Elements of quasi-Bloch states

The current operator in the unperturbed Bloch basis is diagonal: $J_{kk'}^{(0)} = \langle \psi_k^{(0)} | \hat{J} | \psi_k^{(0)} \rangle = \delta_{kk'} J_k^{(0)}$, where $J_k^{(0)} = \partial_k \epsilon_k = 2 \sin(k)$ (for $t = e = \hbar = a = 1$). From Eq. A8 the perturbed current matrix elements are:

$$J_{kk'} = |c_k|^2 J_{k,k'}^{(0)} + \sum_n \left(\frac{W}{2t}\right)^n \left[\sum_{\sigma=\pm 1} \left(c_{k'} \tilde{c}_{k\sigma n} J_{k+\sigma 2\pi n\beta, k'}^{(0)} + \tilde{c}_{k'\sigma n} c_k^* J_{k, k'+\sigma 2\pi n\beta}^{(0)} \right) \right] + \sum_{n,m} \left(\frac{W}{2t}\right)^{n+m} \sum_{\sigma', \sigma=\pm 1} \tilde{c}_{k\sigma n} \tilde{c}_{k'\sigma' m} J_{k+\sigma 2\pi n\beta, k'+\sigma' 2\pi m\beta}^{(0)}. \quad (\text{A9})$$

The perturbed current matrix elements have three distinct terms. The first, represents current coupling between the clean Bloch basis and are weighted by the normalization factor c_k . The second (middle), are off-diagonal terms representing the current coupling between the original Bloch state of $|\psi_k\rangle$ with the higher-order harmonics of $|\psi_{k'}\rangle$ (and vice-versa). The last term represents current coupling between the higher-order harmonics of both perturbed states.

3. Drude Weight from Perturbed Current Matrix Elements

To obtain the Drude weight we need to calculate the Fermi velocity Eq. B8. So, we are interested in the diagonal matrix element $J_k = \langle \psi_k | \hat{J} | \psi_k \rangle$ for the perturbed state. Due to the translation symmetry, the unperturbed current matrix elements are diagonal $J_{kk'}^{(0)} \propto \delta_{kk'}$ and the cross-terms in $J_{kk'}$ vanish. The resulting expression is a weighted sum of the unperturbed current matrix elements:

$$J_k = |c_k|^2 J_k^{(0)} + \sum_n \sum_{\sigma=\pm 1} \left(\frac{W}{2t}\right)^{2n} |\tilde{c}_{k\sigma n}|^2 J_{k+\sigma 2\pi n\beta}^{(0)}. \quad (\text{A10})$$

This is the same expression as Eq. 9 in the main text. This result directly explains the suppression of the Drude weight D . At $T = 0$, $D \propto |v_F| \propto J_{k_F}$ (Appendix. B).

1. For $W = 0$, $c_k = 1$ and all $\tilde{c} = 0$. $J_k = J_k^{(0)}$, which is maximal at $k_F = \pm\pi/2$.
2. As W increases, the normalization factor $|c_k|^2$ (the weight of the original state) decreases as spectral weight is transferred to the harmonics ($|\tilde{c}_{k,\sigma,n}|^2 > 0$).
3. The harmonics $k_F \pm 2\pi n\beta$ are further from the band center, so their current matrix elements $\left| J_{k \pm 2\pi n\beta}^{(0)} \right|$ are smaller than $\left| J_{k_F}^{(0)} \right|$.

The total current J_k is thus a sum where weight is transferred from the maximal term $J_{k_F}^{(0)}$ to progressively smaller terms. This leads to a monotonic supression of J_{k_F} , and therefore D , as $W \rightarrow 2$.

4. Perturbation Theory - Numerical Implementation

In this section, we provide the expressions used for the recursive implementation of time-independent non-degenerate perturbation theory [55]. The recursive implementation allows the calculation of the perturbed eigenfunctions up to order m . We used:

$$\Delta_n^{(N)} = \langle \psi_n^{(0)} | V | \psi_n^{(N-1)} \rangle \quad (\text{A11})$$

$$|\psi_n^{(N)}\rangle = \sum_{i \neq n} \frac{\langle \psi_i^{(0)} | V | \psi_n^{(N-1)} \rangle}{E_n^{(0)} - E_i^{(0)}} |\psi_i^{(0)}\rangle - \sum_{i \neq n} \sum_{m \geq 0} \Delta_n^{(m+1)} \frac{\langle \psi_i^{(0)} | \psi_n^{(N-1-m)} \rangle}{E_n^{(0)} - E_i^{(0)}} |\psi_i^{(0)}\rangle \quad (\text{A12})$$

where $\Delta_n^{(N)}$ is the m -th order correction to the eigenenergy $E_n = E_n^{(0)} + \sum_m \Delta_n^{(m)}$ and $|\psi_n^{(N)}\rangle$ the m -th order correction to the wavefunction $|\psi_n\rangle = |\psi_n^{(0)}\rangle + \sum_m |\psi_n^{(m)}\rangle$.

Appendix B: Drude Weight at $T = 0$

In Sec. III the Drude weight was introduced. For a translationally invariant system, the Hamiltonian is diagonal in the Bloch basis, and Eq. 6 takes the form:

$$D = -\frac{1}{L} \sum_{k \in \text{FBZ}} \frac{\partial f}{\partial \epsilon_k} |J_k|^2. \quad (\text{B1})$$

In the thermodynamic limit ($L \rightarrow \infty$) the sum becomes an integral:

$$D \approx -\frac{1}{2\pi} \int_{\text{FBZ}} dk \frac{\partial f}{\partial \epsilon_k} |J_k|^2. \quad (\text{B2})$$

We can take the zero temperature limit by noting that the Fermi-Dirac derivative becomes a delta function: $-\frac{\partial f}{\partial \epsilon_k} \rightarrow \delta(\epsilon_k - \epsilon_F)$. At half-filling ($\epsilon_F = 0$ for the clean system), the integral is:

$$D = \frac{1}{2\pi} \int_{\text{FBZ}} \delta(\epsilon_k - \epsilon_F) |J_k|^2 dk. \quad (\text{B3})$$

To solve this integral, we use the identity $\delta(g(k)) = \sum_i \frac{\delta(k - k_i)}{|g'(k_i)|}$, where k_i are the roots of $g(k)$. Here, $g(k) = \epsilon_k - \epsilon_F$, and the roots are the Fermi momenta, $k_F = \pm\pi/2$. The derivative is $g'(k) = \partial_k \epsilon_k = v_k$ (the group velocity). At the Fermi points, $|v(\pm\pi/2)| = |v_F|$. The delta function is therefore:

$$\delta(\epsilon_k - \epsilon_F) = \frac{\delta(k - \pi/2)}{|v_F|} + \frac{\delta(k + \pi/2)}{|v_F|}. \quad (\text{B4})$$

Substituting this into Eq. B3 yields:

$$D = \frac{1}{2\pi |v_F|} \int_{\text{FBZ}} [\delta(k - \pi/2) + \delta(k + \pi/2)] |J_k|^2 dk \quad (\text{B5})$$

$$= \frac{1}{2\pi |v_F|} \left(|J_{-\pi/2}|^2 + |J_{\pi/2}|^2 \right). \quad (\text{B6})$$

Since $|J_{-\pi/2}| = |J_{\pi/2}|$, the two Fermi points contribute equally:

$$D = \frac{1}{\pi} \frac{|J_{k_F}|^2}{|v_F|}. \quad (\text{B7})$$

In units of $e = \hbar = a = 1$, the current operator is $J_k = \partial_k \epsilon_k = v_k$. Therefore, $J_{k_F} = v_F$. Substituting into Eq. B7, gives the final well-known result:

$$D = \frac{|v_F|}{\pi} \quad (\text{B8})$$

This result is valid for any 1D system at $T = 0$. For the clean 1D tight-binding chain, the dispersion relation is $\epsilon_k = -2t \cos(k)$, and so we have $|v_F| = |v(k_F = \pm\pi/2)| = 2t$. With $t = 1$, this yields the maximum Drude weight $D = \frac{2}{\pi} \approx 0.637$.

For the AA model with $W < 2$, the system remains ballistic, and the unperturbed momentum k remains a good quantum number. Therefore, Eq. B8 still holds, however, with a W dependent Fermi velocity v_F . As described in Sec. B, this v_F can be obtained either from perturbation theory or from real-space numerical calculations of $J_{k_F} = \langle \psi_{\epsilon_F} | \hat{J} | \psi_{\epsilon_F} \rangle$.

Appendix C: van Hove singularities in 1D

We derive the density of states (DOS) for a 1D tight-binding chain and calculate the scaling of the number of states near a van Hove singularity. The density of states is given by:

$$\rho(E) = \frac{1}{L} \sum_{k \in \text{FBZ}} \delta(E - \epsilon(k)) \quad (\text{C1})$$

$$= \frac{1}{2\pi} \int_{-\pi}^{\pi} \delta(E - \epsilon(k)) dk. \quad (\text{C2})$$

For the 1D chain, $\epsilon(k) = -2t \cos(k)$. Using the identity $\delta(g(k)) = \sum_i \frac{\delta(k - k_i)}{|g'(k_i)|}$, and $\partial_k \epsilon_k = 2t \sin(k)$ leads to the well-known result:

$$\rho(E) = \frac{1}{\pi} \int_0^{\pi} \delta(E + 2t \cos(k)) dk \quad (\text{C3})$$

$$= \frac{1}{2\pi t \sin(\arccos(-\frac{E}{2t}))}. \quad (\text{C4})$$

$$= \frac{1}{\pi \sqrt{(2t)^2 - E^2}} \quad (\text{C5})$$

This expression exhibits a square root divergence at the band edges $E = \pm 2t$, corresponding to the 1D van Hove singularities. Close to the van Hove singularity, we have $\rho(E) \approx \frac{1}{2\pi \sqrt{t} \sqrt{2t - |E|}}$.

We can now determine how the number of states N_{VHS} in an energy window ΔE near the van Hove singularity scales with system size L . We are interested in an energy window ΔE that shrinks with L , specifically $\Delta E \propto \langle S_{\text{ave}} \rangle \propto \frac{1}{L}$, where S_{ave} is the mean level spacing around the Fermi level.

To inspect how the number of states in the singularity changes with system size, we evaluate the following integral,

$$N_{\text{VHS}} = L \int_{2t - \Delta E}^{2t} \rho(E) dE. \quad (\text{C6})$$

Using the approximation $\rho(E) \approx C (2t - |E|)^{-1/2}$ (where C is a constant), we solve the integral:

$$N_{\text{VHS}} \approx L \cdot C \int_{2t - \Delta E}^{2t} (2t - |E|)^{-1/2} dE \quad (\text{C7})$$

$$N_{\text{VHS}} \propto L \cdot \left[-2\sqrt{2t - |E|} \right]_{2t - \Delta E}^{2t} \propto L \sqrt{\Delta E}. \quad (\text{C8})$$

By substituting the scaling of the energy window, $\Delta E \propto L^{-1}$, we obtain the final scaling for the number of states within the singularity:

$$N_{\text{VHS}} \propto L\sqrt{1/L} \propto \sqrt{L}. \quad (\text{C9})$$

This \sqrt{L} scaling is a direct result of the quadratic band edge, and is used in Appendix D to determine the scaling of the conductivity peak.

Appendix D: Conductivity Peak Scaling

At finite temperatures, transitions between adjacent, partially filled van Hove singularities lead to strong resonant peaks in the conductivity. To understand the system-size scaling of these peaks (Fig. 10(c)), we provide a heuristic derivation based on the Kubo-Greenwood formula. In the Kubo-Greenwood expression (Eq. 2), the phenomenological broadening η represents an energy scale below which discrete energy levels are mixed. For a finite system of size L , the mean level spacing $\langle S_{\text{ave}} \rangle$ scales as $\langle S_{\text{ave}} \rangle \propto L^{-1}$. To properly capture the thermodynamic limit, η must be related to this intrinsic energy scale. We thus set the broadening proportional to the mean level spacing: $\eta \propto L^{-1}$.

We simplify our problem by considering only the two resonating van Hove singularities, A and B , separated by ω_{peak} . As shown in Appendix C, the number of states N_{VHS} within a small energy window ΔE from a 1D van Hove singularity diverges as $N_{\text{VHS}} \propto L\sqrt{\Delta E}$. We can approximate the sum in the Kubo formula (Eq. 2) at the resonance $\omega = \omega_{\text{peak}}$ by an average over the current-generating transitions:

$$\sigma_{\text{peak}} = \text{Re}[\sigma_{\text{reg}}(\omega_{\text{peak}})] \approx \frac{(f_1 - f_2) |\langle J_{\text{ave}} \rangle|^2 N_{J \neq 0}}{\eta \omega_{\text{peak}} L}, \quad (\text{D1})$$

where $N_{J \neq 0}$ is the total number of current-generating transitions. As argued in the main text, states in adjacent van Hove singularities are coupled in strong pairwise resonances. Therefore, $N_{J \neq 0} \neq N_{\text{VHS}}^2$, but instead it is proportional to the number of states in a single van Hove singularity, $N_{J \neq 0} \propto N_{\text{VHS}}$. The relevant energy window for these transitions is the broadening η . Thus, the number of contributing states is $N_{J \neq 0} \propto L\sqrt{\Delta E}$. Substituting this into Eq. D1, we find the scaling of the peak:

$$\sigma_{\text{peak}} \propto \frac{1}{L} \frac{|\langle J_{\text{ave}} \rangle|^2 L \sqrt{\eta}}{\eta} \propto \eta^{-1/2}. \quad (\text{D2})$$

For a generic algebraic scaling $\eta \propto L^{-\alpha}$ with $\alpha \geq 0$ we get $\sigma_{\text{peak}} \propto L^{\alpha/2}$ which agrees with our \sqrt{L} scaling if we choose $\eta \propto \langle S_{\text{ave}} \rangle \implies \alpha = 1$. This result, derived from the unique pairwise coupling and van Hove singularities structure of the 1D system, is in excellent agreement with the numerical results presented in Fig. 10(c).

Appendix E: Temperature Evolution of Conductivity

To supplement the analysis of Sec. IV B 2, we provide the detailed evolution of the real part of the regular conductivity, $\text{Re}[\sigma_{\text{reg}}(\omega)]$, as a function of increasing temperature for two representative potential strengths.

For $W \approx 1.8$ (see Fig. 11) increasing the temperature initially smoothes the $T = 0$ spectral features. As T becomes comparable to the relevant energy gaps, strong thermal mixing occurs between states in adjacent, gapped van Hove singularities. This leads to the emergence of a dominant resonant peak, which reaches its maximal intensity at $T \approx 5 \times 10^{-3}$, roughly 60 times larger than its zero-temperature counterpart.

For $W \approx 1.9$ (see Fig. 12), the conductivity exhibits sharper features at low temperature, reflecting the increased fractal nature of the energy spectrum closer to the critical point. As temperature increases, a similar thermal response appears, but its maximum occurs at a lower temperature ($T \approx 3 \times 10^{-3}$) due to the compression of the spectral bands. Furthermore, the opening of smaller, higher-order mid-band gaps creates a hierarchy of resonances. A secondary, lower-frequency peak is activated at $T \approx 5 \times 10^{-4}$. This demonstrates a mechanism for frequency and temperature

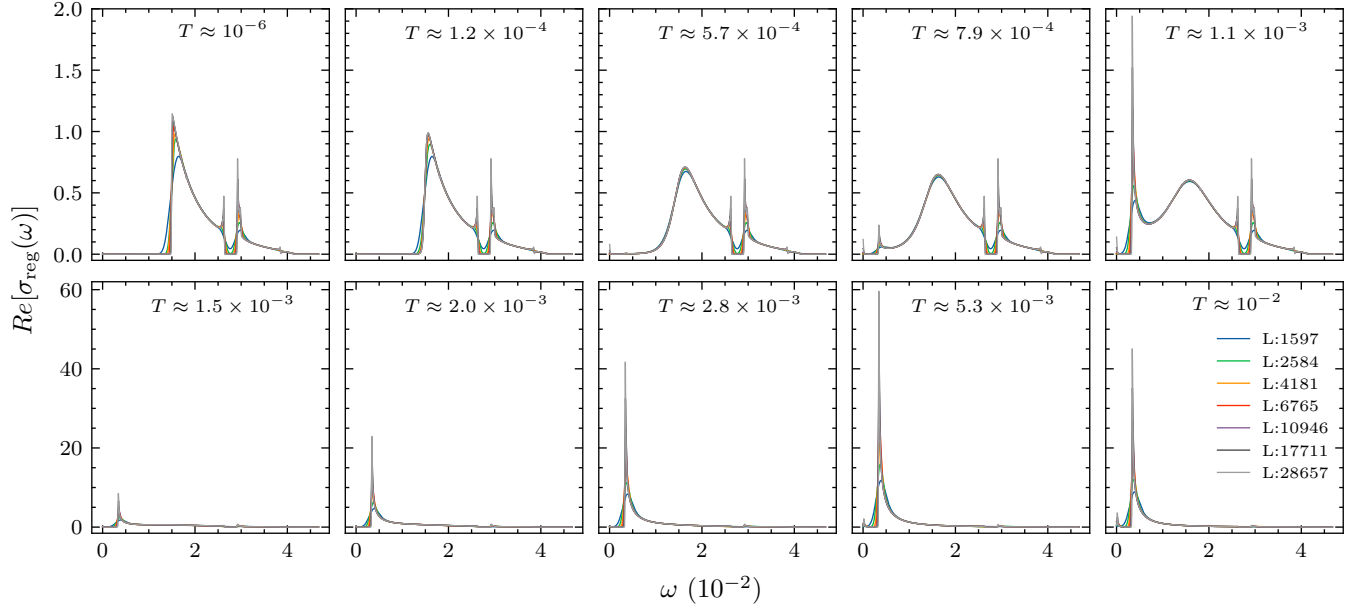


Figure 11. Real part of the regular conductivity ($\text{Re}[\sigma_{\text{reg}}(\omega)]$) as a function of frequency (ω) at $W \approx 1.8$ for different values of increasing temperature. The top and bottom row of plots are on different scales (see y -axis) but share the same scale row wise. The x -axis is shared between all plots.

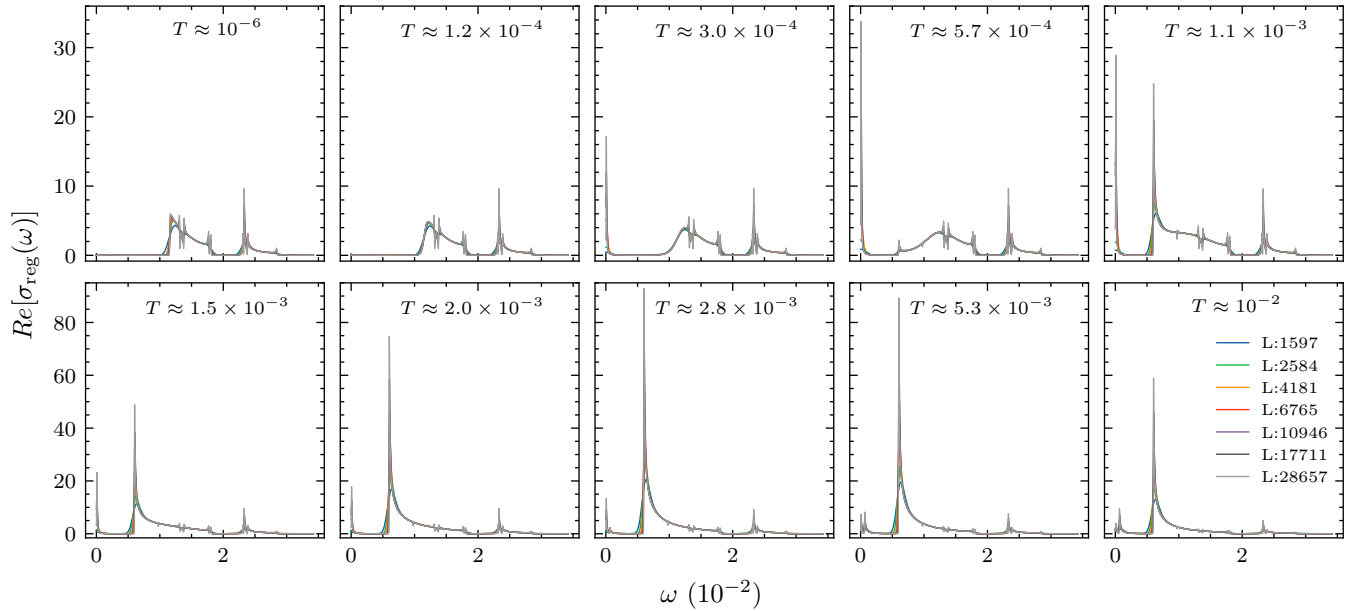


Figure 12. Real part of the regular conductivity ($\text{Re}[\sigma_{\text{reg}}(\omega)]$) as a function of frequency (ω) at $W \approx 1.9$ for different values of increasing temperature. The top and bottom row of plots are on different scales (see y -axis) but share the same scale row wise. The x -axis is shared between all plots.

selective optical transport.

[1] M. Kohmoto, B. Sutherland, and C. Tang, Critical wave functions and a Cantor-set spectrum of a one-dimensional quasicrystal model, *Phys. Rev. B* **35**, 1020 (1987).

- [2] A. I. Goldman and R. F. Kelton, Quasicrystals and crystalline approximants, *Rev. Mod. Phys.* **65**, 213 (1993).
- [3] P. W. Anderson, Absence of Diffusion in Certain Random Lattices, *Phys. Rev.* **109**, 1492 (1958).
- [4] A. MacKinnon and B. Kramer, One-Parameter Scaling of Localization Length and Conductance in Disordered Systems, *Phys. Rev. Lett.* **47**, 1546 (1981).
- [5] S. Aubry and G. André, Analyticity breaking and Anderson localization in incommensurate lattices, *Ann. Israel Phys. Soc.* **3**, 18 (1980).
- [6] Y. E. Kraus, Y. Lahini, Z. Ringel, M. Verbin, and O. Zilberberg, Topological States and Adiabatic Pumping in Quasicrystals, *Phys. Rev. Lett.* **109**, 106402 (2012).
- [7] Y. E. Kraus and O. Zilberberg, Topological Equivalence between the Fibonacci Quasicrystal and the Harper Model, *Phys. Rev. Lett.* **109**, 116404 (2012).
- [8] M. Verbin, O. Zilberberg, Y. E. Kraus, Y. Lahini, and Y. Silberberg, Observation of Topological Phase Transitions in Photonic Quasicrystals, *Phys. Rev. Lett.* **110**, 076403 (2013).
- [9] R. Liquito, M. Gonçalves, and E. V. Castro, Fate of quadratic band crossing under quasiperiodic modulation, *Phys. Rev. B* **109**, 174202 (2024).
- [10] R. Liquito, M. Gonçalves, and E. Castro, Quasiperiodic quadrupole insulators, *SciPost Physics* **18**, 208 (2025).
- [11] R. E. Prange, D. R. Grempel, and S. Fishman, Long-Range Resonance in Anderson Insulators: Finite-Frequency Conductivity of Random and Incommensurate Systems, *Phys. Rev. Lett.* **53**, 1582 (1984).
- [12] N. Roy and S. Sinha, A finite temperature study of ideal quantum gases in the presence of one dimensional quasi-periodic potential, *J. Stat. Mech.* **2018**, 053106 (2018).
- [13] G. Roósz, U. Divakaran, H. Rieger, and F. Iglói, Nonequilibrium quantum relaxation across a localization-delocalization transition, *Phys. Rev. B* **90**, 184202 (2014).
- [14] N. Roy and A. Sharma, Study of counterintuitive transport properties in the Aubry-André-Harper model via entanglement entropy and persistent current, *Phys. Rev. B* **100**, 195143 (2019), [arXiv:1905.13255 \[cond-mat\]](#).
- [15] D. S. Bhakuni, T. L. M. Lezama, and Y. Bar Lev, Noise-induced transport in the Aubry-André-Harper model, *SciPost Phys. Core* **7**, 023 (2024).
- [16] A. Lahiri, Ac conductivity of incommensurate lattices: Anatomy of wave functions, *Phys. Rev. B* **53**, 3702 (1996).
- [17] S. Gopalakrishnan, Self-dual quasiperiodic systems with power-law hopping, *Phys. Rev. B* **96**, 054202 (2017), [arXiv:1706.05382 \[cond-mat\]](#).
- [18] G. Roati, C. D'Errico, L. Fallani, M. Fattori, C. Fort, M. Zaccanti, G. Modugno, M. Modugno, and M. Inguscio, Anderson localization of a non-interacting Bose-Einstein condensate, *Nature* **453**, 895 (2008).
- [19] M. Modugno, Exponential localization in one-dimensional quasi-periodic optical lattices, *New J. Phys.* **11**, 033023 (2009).
- [20] M. Schreiber, S. S. Hodgman, P. Bordia, H. P. Lüschen, M. H. Fischer, R. Vosk, E. Altman, U. Schneider, and I. Bloch, Observation of many-body localization of interacting fermions in a quasirandom optical lattice, *Science* **349**, 842 (2015).
- [21] H. P. Lüschen, P. Bordia, S. Scherg, F. Alet, E. Altman, U. Schneider, and I. Bloch, Observation of Slow Dynamics near the Many-Body Localization Transition in One-Dimensional Quasiperiodic Systems, *Phys. Rev. Lett.* **119**, 260401 (2017).
- [22] R. Anderson, F. Wang, P. Xu, V. Venu, S. Trotzky, F. Chevy, and J. H. Thywissen, Conductivity Spectrum of Ultracold Atoms in an Optical Lattice, *Phys. Rev. Lett.* **122**, 153602 (2019).
- [23] W. G. T. Kamkou, N. Tchepemen, and J. P. Nguenang, Spectral and dynamical characters of 1D incommensurate optical lattices with PT-symmetry, *Physica B: Condensed Matter* **667**, 415130 (2023).
- [24] Y. Lahini, R. Pugatch, F. Pozzi, M. Sorel, R. Morandotti, N. Davidson, and Y. Silberberg, Observation of a Localization Transition in Quasiperiodic Photonic Lattices, *Phys. Rev. Lett.* **103**, 013901 (2009).
- [25] Moiré magic three years on, *Nat Rev Mater* **6**, 191 (2021).
- [26] P. Moon, M. Koshino, and Y.-W. Son, Quasicrystalline electronic states in $\{30\}^{\circ}$ rotated twisted bilayer graphene, *Phys. Rev. B* **99**, 165430 (2019).
- [27] G. Yu, Z. Wu, Z. Zhan, M. I. Katsnelson, and S. Yuan, Dodecagonal bilayer graphene quasicrystal and its approximants, *npj Comput Mater* **5**, 1 (2019).
- [28] S. Pezzini, V. Mišekis, G. Piccinini, S. Forti, S. Pace, R. Engelke, F. Rossella, K. Watanabe, T. Taniguchi, P. Kim, and C. Coletti, 30° -Twisted Bilayer Graphene Quasicrystals from Chemical Vapor Deposition, *Nano Lett* **20**, 3313 (2020).
- [29] M. Gonçalves, H. Z. Olyaei, B. Amorim, R. Mondaini, P. Ribeiro, and E. V. Castro, Incommensurability-induced sub-ballistic narrow-band-states in twisted bilayer graphene, *2D Mater.* **9**, 011001 (2021).
- [30] A. Uri, S. C. de la Barrera, M. T. Randeria, D. Rodan-Legrain, T. Devakul, P. J. D. Crowley, N. Paul, K. Watanabe, T. Taniguchi, R. Lifshitz, L. Fu, R. C. Ashoori, and P. Jarillo-Herrero, Superconductivity and strong interactions in a tunable moiré quasicrystal, *Nature* **620**, 762 (2023).
- [31] X. Lai, D. Guerci, G. Li, K. Watanabe, T. Taniguchi, J. Wilson, J. H. Pixley, and E. Y. Andrei, *Imaging Self-aligned Moiré Crystals and Quasicrystals in Magic-angle Bilayer Graphene on hBN Heterostructures* (2023), [arXiv:2311.07819 \[cond-mat\]](#).
- [32] M. Gonçalves, B. Amorim, E. V. Castro, and P. Ribeiro, Critical Phase Dualities in 1D Exactly Solvable Quasiperiodic Models, *Phys. Rev. Lett.* **131**, 186303 (2023).
- [33] R. Oliveira, N. Sobrosa, P. Ribeiro, B. Amorim, and E. V. Castro, *Local Density of States as a Probe of Multifractality in Quasiperiodic Moiré Materials* (2025), [arXiv:2510.20575 \[cond-mat\]](#).
- [34] A. Purkayastha, S. Sanyal, A. Dhar, and M. Kulkarni, Anomalous transport in the Aubry-André-Harper model in isolated and open systems, *Phys. Rev. B* **97**, 174206 (2018).
- [35] Y. Bar Lev, D. M. Kennes, C. Klöckner, D. R. Reichman, and C. Karrasch, Transport in quasiperiodic interacting systems: From superdiffusion to subdiffusion, *EPL* **119**, 37003 (2017).

- [36] J. Sutrardhar, S. Mukerjee, R. Pandit, and S. Banerjee, Transport, multifractality, and the breakdown of single-parameter scaling at the localization transition in quasiperiodic systems, *Phys. Rev. B* **99**, 224204 (2019), arXiv:1810.12931 [cond-mat].
- [37] H. Iijima, Y. Murakami, and A. Koga, Optical Response of the Tightbinding Model on the Fibonacci Chain, *J. Phys. Soc. Jpn.* **91**, 124702 (2022).
- [38] N. F. Mott, Conduction in non-crystalline materials: III. Localized states in a pseudogap and near extremities of conduction and valence bands, *The Philosophical Magazine: A Journal of Theoretical Experimental and Applied Physics* **19**, 835 (1969).
- [39] A. Avila and S. Jitomirskaya, The Ten Martini Problem, *Ann. Math.* **170**, 303 (2009).
- [40] R. Kubo, Statistical-Mechanical Theory of Irreversible Processes. I. General Theory and Simple Applications to Magnetic and Conduction Problems, *J. Phys. Soc. Jpn.* **12**, 570 (1957).
- [41] D. A. Greenwood, The Boltzmann Equation in the Theory of Electrical Conduction in Metals, *Proc. Phys. Soc.* **71**, 585 (1958).
- [42] I. Souza, T. Wilkens, and R. M. Martin, Polarization and localization in insulators: Generating function approach, *Phys. Rev. B* **62**, 1666 (2000).
- [43] R. Resta, Why are insulators insulating and metals conducting?, *J. Phys.: Condens. Matter* **14**, R625 (2002).
- [44] R. Resta, Drude weight and superconducting weight, *J. Phys.: Condens. Matter* **30**, 414001 (2018).
- [45] P. Drude, Zur Elektronentheorie der Metalle, *Annalen der Physik* **306**, 566 (1900).
- [46] D. J. Scalapino, S. R. White, and S. Zhang, Insulator, metal, or superconductor: The criteria, *Phys. Rev. B* **47**, 7995 (1993).
- [47] J. Zhang, X. Chen, S. Mills, T. Ciavatti, Z. Yao, R. Mescall, H. Hu, V. Semenenko, Z. Fei, H. Li, V. Perebeinos, H. Tao, Q. Dai, X. Du, and M. Liu, Terahertz Nanoimaging of Graphene, *ACS Photonics* **5**, 2645 (2018).
- [48] R. Jing, Y. Shao, Z. Fei, C. F. B. Lo, R. A. Vitalone, F. L. Ruta, J. Staunton, W. J.-C. Zheng, A. S. Mcleod, Z. Sun, B.-y. Jiang, X. Chen, M. M. Fogler, A. J. Millis, M. Liu, D. H. Cobden, X. Xu, and D. N. Basov, Terahertz response of monolayer and few-layer WTe₂ at the nanoscale, *Nat Commun* **12**, 5594 (2021).
- [49] X. Guo, K. Bertling, B. C. Donose, M. Brünig, A. Cernescu, A. A. Govyadinov, and A. D. Rakić, Terahertz nanoscopy: Advances, challenges, and the road ahead, *Applied Physics Reviews* **11**, 021306 (2024).
- [50] S.-D. Chen, Q. Feng, W. Zhao, R. Qi, Z. Zhang, D. Abeyasinghe, C. Uzundal, J. Xie, T. Taniguchi, K. Watanabe, and F. Wang, Direct measurement of terahertz conductivity in a gated monolayer semiconductor, <https://arxiv.org/abs/2409.17633v1> (2024).
- [51] W. Kohn, Theory of the Insulating State, *Phys. Rev.* **133**, A171 (1964).
- [52] D. Thouless, Electrons in disordered systems and the theory of localization, *Physics Reports* **13**, 93 (1974).
- [53] This holds for resonating pairs around gapped van Hove singularities.
- [54] Note that within the localized phase ($W > 2$), a large W perturbative expansion can also be carried out, treating the hopping as a perturbation. In this case, gap openings are induced by real-space resonances (and not momentum-space resonances like in the extended phase).
- [55] J. J. Sakurai and J. Napolitano, *Modern Quantum Mechanics*, 3rd ed. (Cambridge University Press, Cambridge, 2021).